JGR Planets

RESEARCH ARTICLE

10.1029/2026JE009904

Rheology and Structure of Fe-Mg-Ca Enriched Silicate Melt: Benchmarking Viscosity Models for an Exotic Planetary Composition

Fabrizio Di Fiore[1] and **Michele Cassetta**[2]

[1]Istituto Nazionale di Geofisica e Vulcanologia (INGV), Rome, Italy, [2]Department of Engineering for Innovation Medicine, University of Verona, Verona, Italy

Key Points:

- Extraterrestrial melts rich in iron, calcium, and magnesium are more depolymerized and less viscous than typical terrestrial basalts
- Traditional semi-empirical models fail to accurately predict the viscosity of exotic and ultramafic planetary compositions
- Model based on atomic vibrations provides better accuracy in predicting viscosity of melt across temperatures investigated in this study

Correspondence to:

F. Di Fiore and M. Cassetta,
fabrizio.difiore@ingv.it;
michele.cassetta@univr.it

Citation:

Di Fiore, F., & Cassetta, M. (2026). Rheology and structure of Fe-Mg-Ca enriched silicate melt: Benchmarking viscosity models for an exotic planetary composition. *Journal of Geophysical Research: Planets*, *131*, e2026JE009904. https://doi.org/10.1029/2026JE009904

Received 13 MAY 2026
Accepted 30 JUL 2026

Author Contributions:

Conceptualization: Fabrizio Di Fiore, Michele Cassetta
Data curation: Fabrizio Di Fiore, Michele Cassetta
Formal analysis: Fabrizio Di Fiore, Michele Cassetta
Funding acquisition: Fabrizio Di Fiore, Michele Cassetta
Investigation: Fabrizio Di Fiore, Michele Cassetta
Methodology: Fabrizio Di Fiore, Michele Cassetta
Resources: Fabrizio Di Fiore, Michele Cassetta
Validation: Fabrizio Di Fiore, Michele Cassetta
Visualization: Fabrizio Di Fiore, Michele Cassetta

Abstract Silicate melt viscosity plays a pivotal role in the evolution of rocky bodies within the Solar System, exerting first-order control on mantle differentiation and stratification, while dictating the metal-silicate separation and the subsequent volcanic activity. Thus, predicting the viscosity of planetary compositions is essential to model and better understand their thermomechanical evolution. Notably, the chemical signatures of primordial planetary magmas, marked by extreme Fe, Mg, and Ca enrichment, drive a highly depolymerized and fragile rheological regimes that frequently fall beyond the calibration data sets used to model the viscosity. In this study, we characterize the effect on viscosity by doping a basalt with iron, magnesium, and calcium to resemble an exotic planetary composition. By integrating high- and low-temperature viscometry with Raman spectroscopy and ultrasonic data, we show that this chemical enrichment significantly impacts the rheology, elasticity and the structural organization of the doped melt. In particular, viscosity decreases ∼2 times at high temperatures compared to the original basalt. This behavior is driven by the extreme depolymerization of the melt, and it is reflected in a shift toward Q^2 and Q^1 structural units. Vibrational analysis via the Boson Peak confirms a highly fragile state characterized by noticeably small correlation lengths. We tested several widely used semi-empirical models and found that while traditional empirical formulations struggle to accurately predict the viscosity of these exotic compositions, spectroscopy-based frameworks provide significantly better accuracy. This performance highlights the fundamental link between atomic-scale vibrational properties and melt-scale dynamics.

Plain Language Summary Understanding how molten rock (magma) flows is essential for learning how planets form and how volcanoes erupt. The ability of magma to flow (i.e., its viscosity) determines how a young planet separates into layers, such as core and mantle. Most current tools for predicting magma viscosity are primarily based on databases generated from terrestrial rocks. However, certain early planets and meteorites may contain much higher chemical concentrations of iron, magnesium, and calcium than typical Earth rocks. In this study, we synthesized a molten rock in the lab to mimic one of these "exotic" planetary compositions, by adding iron, magnesium, and calcium to a basalt (one of the most common rocks on the Earth surface). We discovered that this chemical composition makes the magma flow much more easily than parent-basalt. We also found that traditional models struggle to predict this behavior accurately because they were not calibrated for such extreme chemistry. Instead, a method that looks at how atoms vibrate within the material provided much more reliable results. This research shows that understanding the atomic-scale structure of magma is a powerful way to predict their characteristics such as viscosity, which in turn are essential to model and understand large-scale planetary evolution.

1. Introduction

Viscosity is one of the fundamental physical properties governing the magmatic evolution and tectonics of rocky planetary bodies (Lark et al., 2024; Marchi et al., 2023; Marchi and Korenaga, 2025; Russell et al., 2022). In magmatic systems, the pure liquid phase of silicate melts represents the host matrix in which crystal nucleation and growth occur, and through which chemical diffusion and heat transfer are mediated. The viscosity of the liquid phase therefore governs the kinetics of crystallization and subsequent settling, metallic segregation, and chemical differentiation, ultimately exerting a first-order control on the thermal and structural evolution of planetary interiors (Breuer et al., 2022; Demidova & Badyukov, 2023; Herzberg et al., 2010; Lark et al., 2024; Marchi et al., 2023; Weiss & Elkins-Tanton, 2013). In this context, obtaining robust predictions for magma

Writing – original draft: Fabrizio Di Fiore, Michele Cassetta
Writing – review & editing: Fabrizio Di Fiore, Michele Cassetta

rheology is crucial, as highlighted by Russell et al. (2022) in their recent review of the available viscosity models for geological melts.

Furthermore, complementary elastic properties provide an additional and independent probe of melt structure, linking atomic-scale organization to macroscopic mechanical behavior and offering key constraints on the microstructural state of the liquid (Cassetta et al., 2026; Lin and Liu, 2006; Pisello et al., 2025; Su et al., 2025; Wu et al., 2014).

During the early planetary melting phase, magma oceans formed, and the physical properties of the liquid phase dictated the establishment of primordial mantle stratification (Boukarè et al., 2025; Schaefer & Elkins-Tanton, 2018). As cooling and crystallization progress, melt viscosity governed the dynamics of melt extraction, transport, and emplacement. Beyond the subsurface, viscosity modulated planetary volcanism by dictating eruptive intensity and the resulting morphology of lava flows, from differentiated asteroids (e.g., Vesta) to the rocky planets (Boukarè et al., 2025; Demidova & Badyukov, 2023; Hamano et al., 2013). Together, viscosity, vibrational and elastic properties establish critical structure–property relationships that connect melt composition and microstructure to the large-scale evolution of rocky bodies. Robust experimental constraints on these properties are therefore essential for linking melt-scale processes to the macroscopic structure of planetary interiors.

The chemical compositions of primordial planetary magmas are typically silica-undersaturated (<45 wt%) and enriched in Fe together with alkaline earth elements such as Mg and Ca, as suggested by chondritic and angritic meteorites (Demidova & Badyukov, 2023; Goodrich & Delaney, 2000; Keil, 2012; Kleine et al., 2012; Weiss & Elkins-Tanton, 2013). These compositions differ significantly from the terrestrial melts used to calibrate most of the existing viscosity models (e.g., Cassetta et al., 2021; Giordano et al., 2008; Hui & Zhang, 2007; Langhammer et al., 2022; Le Losq et al., 2025; Sehlke & Whittington, 2016), leading to large uncertainties when extrapolated to ultramafic and extraterrestrial systems. Furthermore, silica poor melts are characterized by low viscosities and fast crystallization kinetics (Arzilli et a., 2019; Di Fiore et al., 2022; Di Fiore, Vona, Mollo et al., 2023; Di Fiore, Vona, Scarani et al., 2023; Giuliani et al., 2025; Verdurme et al., 2023), hindering the characterization of the pure liquid phase at *subliquidus* temperatures (e.g., Di Genova, Brooker et al., 2020; Scarani et al., 2022; Valdivia et al., 2025). Consequently, to ensure data reliability it is necessary to carry out rigorous spectroscopic characterization of the sample to rule out the presence of nano-heterogeneities and nanolites that would invalidate the viscosity results (Cassetta et al., 2026; Di Genova, Zandona, & Deubener, 2020; Giuliani et al., 2024; Szewczyk & Cassetta, 2024; Scarani et al., 2022; Valdivia et al., 2025; Verdurme et al., 2023; Zandonà et al., 2023).

Here, we synthesized an exotic silica-undersaturated melt by chemically doping a natural Icelandic MORB, to investigate how the compositional enrichment in iron, magnesium and calcium influences the physical behavior of the liquid matrix. Viscosity measurements performed across a broad *supersolidus* temperature range were combined with Raman spectroscopy and elastic property determinations to directly relate liquid composition to microstructural organization and mechanical response. The rheological effects of Fe-Mg-Ca enrichment were quantified through comparison with the parental basalt and evaluated against existing semi-empirical viscosity models. Our results highlight the need for new experimental data sets on compositionally extreme melts and provide improved constraints for modeling the accretion, differentiation, and early evolution of rocky planetary bodies.

2. Materials and Methods

2.1. Sample Preparation

The starting material used in this study was a basalt from the 1984 lava flow at Krafla volcano (Iceland, Tryggvason, 1986).

First, lava blocks were broken down into centimeter-sized fragments and subsequently pulverized into a fine powder (<1 mm) utilizing both a jaw crusher and a ring mill. Following the procedure reported in Giuliani et al. (2024), the glassy material was re-powdered in a ball mill, grounded to pass through a #200 mesh sieve and, afterward, doped with pure-grade reagents (FeO, MgO and $CaCO_3$) from Sigma-Aldrich. Both the undoped and doped powder were completely melted into a Fe-presaturated Pt crucible at 1450°C within a Nabertherm® furnace installed at the Experimental Volcanology and Petrology Laboratory (EVPLab) of the University of Roma Tre in Rome (Italy). In detail, the powdered samples were added to the crucible in batches of approximately 10–15 g every 10 min, to avoid the overflow of the melt due to foaming. When the crucible was completely filled,

Table 1
Major Element Chemical Compositions (wt.%) of the Starting Material and the Doped Sample (Pre- and Post-Experimental Runs)

	Starting material		Doped material			
			(Pre-run)		(Post-run)	
Oxide	wt.%	s.d.	wt.%	s.d.	wt.%	s.d.
SiO_2	50.94	0.27	42.46	0.31	42.37	0.35
TiO_2	2.02	0.03	1.68	0.04	1.64	0.04
Al_2O_3	13.74	0.16	11.45	0.15	11.52	0.18
FeO	13.71	0.15	16.90	0.15	16.85	0.16
MnO	0.25	0.02	0.21	0.02	0.21	0.02
MgO	5.94	0.11	9.95	0.13	10.01	0.13
CaO	10.02	0.12	14.53	0.14	14.48	0.16
Na_2O	2.49	0.05	2.08	0.05	2.05	0.05
K_2O	0.32	0.03	0.27	0.02	0.28	0.02
P_2O_5	0.56	0.02	0.46	0.03	0.46	0.03

Note. Standard deviations (s.d.) are reported for each oxide.

the molten materials were maintained at this temperature for approximately ~2 hr before being rapidly quenched in water to form a glass.

An aliquot of both the pristine glass and the doped glass were used to carry out chemical analysis using a Jeol JXA-iSP-100 electron probe microanalyzer (EPMA) equipped with five wavelength dispersive spectrometers at the High Pressures–High Temperatures Laboratory of Experimental Volcanology and Geophysics (HP-HT Lab) of the Istituto Nazionale di Geofisica e Vulcanologia (INGV) in Rome (Italy). In detail, the analyses were carried out on carbon-coated samples under high vacuum conditions, using an accelerating voltage of 15 kV and an electron beam current of 10 nA, with a beam diameter of 5 μm. Elemental counting times were 20 s on the peak and 10 s on each of the two background positions. Corrections for interelemental effects were made using a ZAF (Z: atomic number; A: absorption; F: fluorescence) procedure. Calibration used a range of standards from Micro-Analysis Consultants (MAC; https://www.macstandards.co.uk): albite (Si-PET, Al-TAP, Na-TAP), forsterite (Mg-TAP), augite (Fe-LIF), apatite (Ca-PET), orthoclase (K-PET), rutile (Ti-PET) and rhodonite (Mn-LIF). To avoid alkali migration effects, Na and K were analyzed first. BCR-2 was used as a quality monitor standard during the analyses. Based on counting statistics, accuracy was better than 1%–5%, except for elements with abundances below 1 wt%, for which accuracy was better than 5%–10%. Precision was typically better than 1%–5% for all analyzed elements. The chemical composition of the starting material is reported in Table 1. In addition, to verify the chemical stability of the melt and rule out any compositional changes during the experiments (e.g., iron migration and/or alkali loss), EPMA analyses were carried out on the post-run glass products (Table 1).

2.2. High-*T* Liquid Viscosity

High-*T* viscosity measurements of the synthesized doped glass were performed using a Concentric Cylinder (CC) apparatus at the Laboratory of Experimental Volcanology and Petrology (EVPLab) of Roma Tre University. The CC setup includes a Rheotronic II Rotational Viscometer (Theta Instruments) with an Anton Paar RheolabQc viscometer head (full-scale torque of 75 mNm), a S-type thermocouple (with an accuracy of ±2°C), a $Pt_{80}Rh_{20}$ cylindric crucible (62, 32, and 1.5 mm in height, inner diameter, and wall thickness, respectively) and a $Pt_{80}Rh_{20}$ spindle (3.2 and 42 mm in diameter and length, respectively). To prevent Fe loss from the melt, the $Pt_{80}Rh_{20}$ cylindric crucible and the $Pt_{80}Rh_{20}$ spindle utilized for the high-*T* viscosity measurements were Fe-presaturated. The procedure of calibration of the CC apparatus and the related precision are detailed reported in Di Fiore and Vona (2026). The quenched glass shards were loaded into the $Pt_{80}Rh_{20}$ crucible and completely re-melted at ~1,430°C. The molten material in the crucible was constantly stirred at a shear rate ($\dot{\gamma}$) of 20 s^{-1} under ambient pressure (i.e., 1 atm) and air redox conditions (i.e., $\log fO_2$ of −0.68 bars), starting from a *superliquidus* temperature (*T*) of ~1,430°C for ~2 hr in order to ensure the thermal and chemical homogenization of the melt. Subsequently, the furnace temperature was gradually reduced to reach the desired target *T*: 1,428–1,398–1,373–1,348–1,326–1,299°C. The apparent viscosity (η_a) of the sample at each target *T* is calculated as follows:

$$\eta_a = \frac{\tau}{\dot{\gamma}}, \quad (1)$$

where τ is the shear stress (in Pa) and it is determined by the measured torque at the inner cylinder and $\dot{\gamma}$ is the shear rate applied (in s^{-1}). For each *T*, the apparent viscosity (η_a) of the melt was measured for ~45–60 min, until the achievement of a stable torque and temperature reading during measurement.

2.3. Low-*T* Liquid Viscosity

The melt viscosity at low temperature was derived using Differential Scanning Calorimetry (DSC) measurements. This technique monitors the structural relaxation process occurring at the glass transition interval by examining

the heat flow signal of the glass under controlled temperature. Analysis of the calorimetric traces yields two characteristic temperatures: T^{DSC}_{onset} and T^{DSC}_{peak}. By applying a parallel shift factor (Gottsmann et al., 2002; Stevenson et al., 1995; Giordano and Russell (2007); Di Genova, Brooker et al., 2020), the non-Arrhenian dependence of T^{DSC}_{onset} and T^{DSC}_{peak} on cooling rate (q) can be overlaid on the non-Arrhenian temperature dependence viscosity (η) (Stabile et al., 2021 and reference therein). Consequently, T^{DSC}_{onset} and T^{DSC}_{peak} can be associated with melt viscosity values using the following equation:

$$\text{Log}\ \eta\left(T^{DSC}_{onset,peak}\right) = K_{onset,peak} - \text{Log}(|q|). \quad (2)$$

The DSC measurements were carried out on shards of the previously synthesized doped glass quenched in water (20 ± 5 mg) using a Netzsch Pegasus 404 DSC instrument. These measurements were performed in $PtRh_{20}$ crucibles under N_2 5.0 atm with a flow rate of 25–80 ml/min. The samples were subjected to matching cooling and heating rates of 5, 10 and 20°C/min. For a detailed calibration procedure see Scarani et al. (2022). The parallel shift factor values used to obtain viscosity values were obtained by Di Genova, Brooker et al. (2020) (specifically, $K_{onset} = 11.20$ and $K_{peak} = 9.78$). While these shift factors (K) were calibrated on less depolymerized melts, it is important to consider that applying these K values to the Fe-Mg-Ca rich composition presented in this study might introduce a systematic uncertainty in the low-T viscosity estimates (Di Genova, Brooker et al., 2020). The absence of crystals in the pre- and post-run glasses was confirmed through Raman spectroscopy analyses.

2.4. Raman Spectroscopy (Full and Low-Frequency)

Raman spectroscopy was carried out at the University of Verona in the Center for Technological Platforms (CPT), by means of two spectrometers in order to cover the full spectral range as follows:

1. Unpolarized Raman spectra in the 200–1,300 cm^{-1} range were collected using a Thermo Scientific DXR2 spectrometer, equipped with a solid-state laser operating at an excitation wavelength of 532 nm and an edge filter to suppress the Rayleigh line. The scattered light was analyzed with a high-resolution grating (1,800 grooves) and recorded by a thermoelectrically cooled CCD detector, achieving an average spectral resolution of 2.9 cm^{-1}.
2. Raman measurements below 200 cm^{-1} were performed in crossed polarization (HV) using a Horiba Jobin Yvon T-64000 triple-axis spectrometer in back-scattering geometry. The system was set with three holographic gratings (1,800 lines/mm) in double-subtractive configuration and a liquid-nitrogen-cooled CCD detector (1,024 × 256 pixels), yielding a spectral resolution of about 0.6 cm^{-1} per pixel. Excitation was provided by a Cobolt Fandango 04-DPL solid-state laser at 514.4 nm (50 mW), with the laser power on the sample limited to 10 mW (see details in Enrichi et al., 2023).

2.5. Elastic Properties

To measure the elasticity of the sample we used a double polished prismatic specimen with surface dimensions of approximately 8.0 × 9.5 mm and a thickness of about 3.0 mm. The longitudinal (v_l) and transverse (v_t) sound velocities were determined from the propagation times of longitudinal and transverse acoustic waves, respectively. The propagation times were measured with an accuracy of ±1 ns using piezoelectric transducers (Echometer 1,077, Karl Deutsch), operating in the frequency range of 8–12 MHz and equipped with a DS 6 PB 4–14 probe.

The sample density (ρ) was determined using Archimedes' principle, by comparing the weight measured in air with the apparent weight in water, and it was independently verified by the mass-to-volume ratio calculated from the prismatic geometry of the specimen. Elastic moduli were calculated and reported in Table 2. Elastic moduli were calculated and reported in Table 2 (see also Di Fiore & Cassetta, 2026).

3. Results

3.1. Chemical Analyses

The chemical analyses carried out via Electron Probe Micro-Analyzer (EPMA) confirm that chemical doping effectively shifted the starting basalt toward a Fe-Mg-Ca–enriched composition (Table 1). Furthermore, the comparison of the pre- and post-run analyses rules out that no significant chemical changes occurred during the

Table 2
Longitudinal and Transverse Sound Velocities (v_l and v_t) Calculated Elastic Moduli (G, K, M, E), Poisson's Ratio (σ)

	KRD
v_l (m s^{-1})	6,618 (21)
v_t (m s^{-1})	3,785 (11)
ρ (g cm^{-3})	2.831 (3)
M (GPa)	124.0 (8)
G (GPa)	40.6 (2)
K (GPa)	69.9 (8)
E (GPa)	102.0 (5)
σ	0.26 (3)

Note. In brackets is reported the uncertainty referring to the last significant digits.

rheological measurements (Table 1). In the doped glass, FeO increases to 16.90 wt% (from 13.71 wt%), CaO to 14.53 wt% (from 10.02 wt%), and MgO to 9.95 wt% (from 5.94 wt%), documenting the intended enrichment in refractory network modifiers. The addition of these oxides produces a dilution-driven decrease in the remaining major components, most notably SiO_2 (from 50.94 to 42.46 wt%), with concomitant reductions in Al_2O_3 (from 13.74 to 11.45 wt%) and TiO_2 (from 2.02 to 1.68 wt%); minor oxides decrease proportionally (e.g., MnO = 0.21 wt%, P_2O_5 = 0.46 wt%). Comparison with angrite compositions shows that the resulting melt reaches an "exotic" Fe–Mg–Ca range relative to typical terrestrial basalts, while retaining a non-negligible alkali budget of ~2 wt% (Na_2O = 2.08 wt%, K_2O = 0.27 wt%), higher than most natural angrites (Keil, 2012). Despite this discrepancy, the resulting material provides a melt with concentrations that fall well outside the data sets used by classical empirical models, offering a unique opportunity for rheological characterization of an extraterrestrial chemical composition (Figure 1).

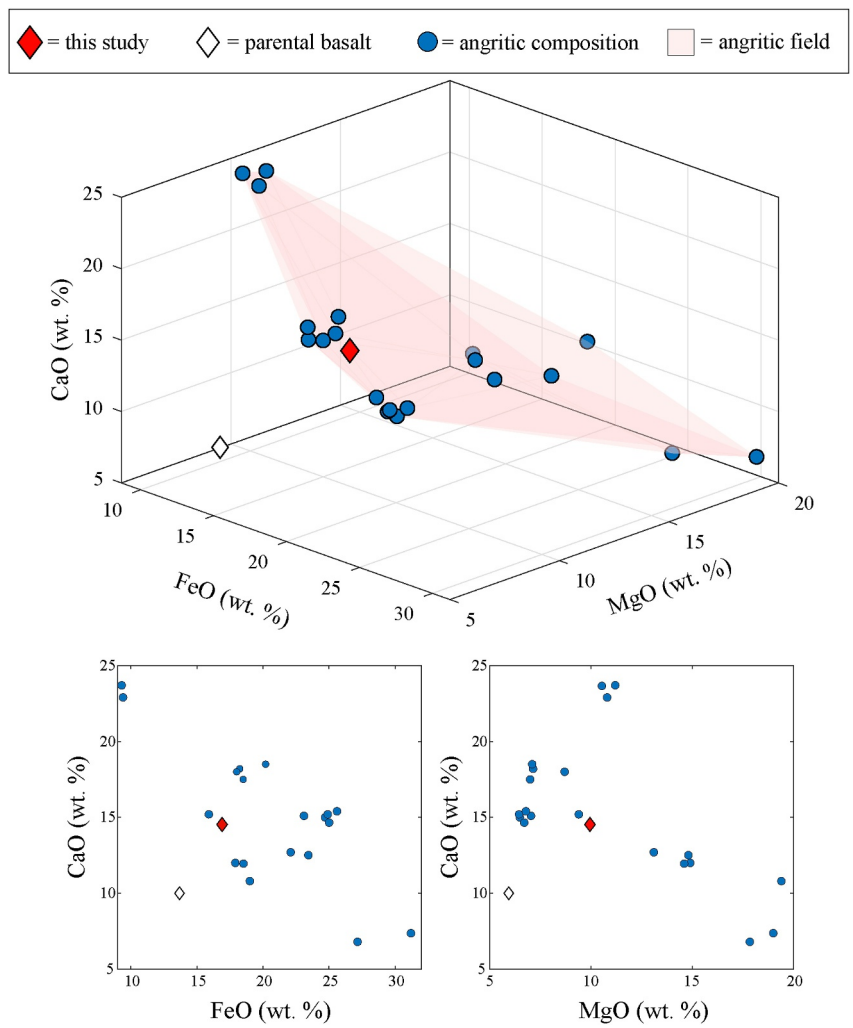

Figure 1. FeO-MgO-CaO compositional space of the doped melt compared with the parental basalt along with the angritic composition field. The red diamond marks the composition investigated in this study, the white diamond the parental basalt whereas the blue circles represent angritic compositions from the literature (see Keil, 2012). The shaded field outlines the compositional domain of angrites. The 3D diagram and its 2D projections show that the doped synthesized melt shifts toward an Fe-Mg-Ca-enriched, chemically exotic planetary-like composition.

Table 3
Viscosity Data of the Anhydrous KRD Melt From Concentric Cylinder (CC) and Differential Scanning Calorimetry (DSC) Measurements

Technique	T (°C)	T (K)	η_a Log (Pa s)
CC	1428	1701	0.26
CC	1398	1671	0.37
CC	1373	1646	0.49
CC	1348	1621	0.61
CC	1326	1599	0.79
CC	1299	1572	0.97
DSC	678	951	10.24
DSC	670	943	10.56
DSC	666	939	10.90
DSC	645	918	11.67
DSC	642	915	11.98
DSC	639	912	12.24
VFT fitting parameters	A	B	C
	−3.88	4,488	632.7

Note. VFT equation parameters obtained by data fitting are also reported.

3.2. Crystal-Free Melt Viscosity

Results from measurements of the crystal-free melt viscosity (η_{liquid}) are reported in Table 3 and in Figure 2. In detail, the high-T viscosity measurements carried out with the Concentric Cylinder (CC) apparatus display η_{liquid} values from Log 0.26 to Log 0.97 Pas with decreasing T from 1,428 to 1,299°C. Measurements performed at T of 1,260°C were discarded due to no constant reading of the torque, indicating a liquidus temperature below T of 1,299°C. Due to the low viscosity of the melt and the high shear rate applied, the flow during the measurements was verified to be under strictly laminar conditions. Based on our lowest viscosity value (Log η = 0.26 Pas at 1,428°C, Table 3), a Reynolds number (Re) of 0.35 was obtained, ensuring a pure Newtonian regime and ruling out any turbulent artifacts during the high-T runs. Such low Re values are typical for low-viscosity silicate melts, as documented in previous works (Di Fiore et al., 2026; Glazner, 2014).

At low-T, the η_{liquid} values estimated from Differential Scanning Calorimeter (DSC) analyses range from Log 10.24 to Log 12.24 Pas, with decreasing T from 678 to 639°C. The η_{liquid} values obtained from both high-T and low-T measurements were fitted via the Vogel-Fulcher-Tammann (VFT) equation (Tammann & Hesse, 1926):

$$\text{Log } \eta = A + B/(T_k - C), \quad (3)$$

where A, B, and C are fitting parameters, and T_k is the temperature in Kelvin. The fitting parameters values are reported in Table 3. The VFT fit reproduces the measured data with a Root Mean Squared Relative Error (RMSRE) of ±0.08 Log units (Figure 2).

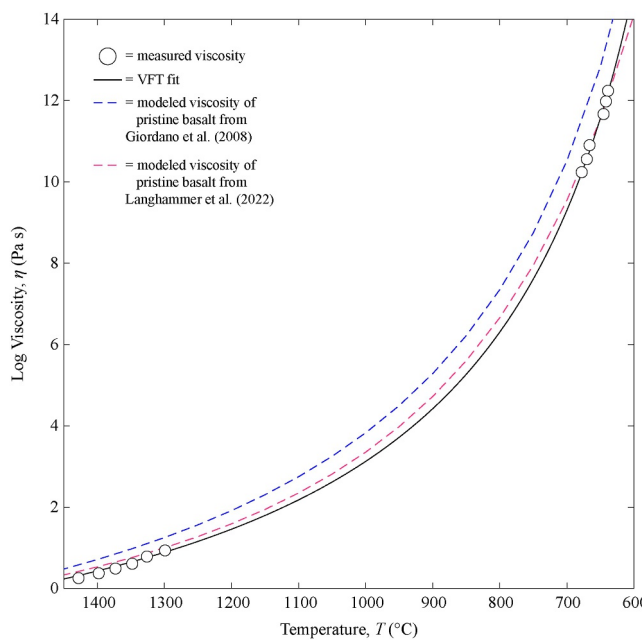

Figure 2. Temperature dependence of viscosity for the doped melt and comparison with the parental basalt viscosity estimated with Giordano et al. (2008, blue dashed line) and Langhammer et al. (2022, red dashed line). Open circles represent measured liquid viscosities obtained from high-temperature concentric-cylinder viscometry and low-temperature DSC-derived estimates. The solid black line is the VFT fit to the experimental data.

3.3. Raman Spectroscopy

The full-range Raman spectrum (Figure 3a) displays a low-intensity ring region (R band Le Losq et al., 2013), which is displaying an envelope at approximately 560 cm^{-1}. This shift indicates a significant population of small-membered rings within the silicate network. In contrast, the stretching region (850–1,250 cm^{-1}) is particularly prominent, exhibiting an intensity that is approximately 190% higher (in terms of relative counts) than that of the *R* band. This marked dominance of the stretching vibrations is consistent with a highly depolymerized network structure dominated by non-bridging oxygen–bearing units (Galeener, 1979).

The high-frequency Raman region (800–1,200 cm^{-1}) was deconvoluted into three Gaussian bands assigned to Q^1, Q^2, and Q^3 structural units. Q^0 species were not included because the estimated NBO/T (~1.4) predicts a silicate network dominated by Q^2 units, with subordinate Q^1 and Q^3 species, while a significant Q^0 population is not expected. Consistently, the introduction of an additional Q^0 component did not result in any significant improvement of the fit (Le Losq & Sossi, 2023). Following, the contribution from Q^4 species is also not predicted due to the highly depolymerized nature of the melt (Figure 3b). This choice is consistent with the elevated NBO/T value and with the absence of a significant fully polymerized silicate framework. We also neglected the asymmetric stretching of bridging oxygens in Q^n units, the so called T^{2s} or BO (Le Losq et al., 2013; Le Losq & Sossi, 2023; Mysen et al., 1982). The relative abundance of each Q^n species was estimated from the integrated area (A) of the corresponding Raman band. Thus the best-fit components are centered at 883.1 cm^{-1} (Q^1), 947.5 cm^{-1} (Q^2), and 1032.3 cm^{-1} (Q^3), with progressively decreasing relative abundance from Q^2 to Q^1 and Q^3. In particular, the dominant Q^2 population ($A \approx 0.55$) indicates a network largely composed of chain-like silicate units, while the presence of Q^1 units ($A \approx 0.15$) reflects terminal tetrahedra associated with abundant network-modifying cations. The limited contribution of Q^3 species ($A \approx 0.30$) further confirms the suppression of extended polymerized domains. The relatively large full width at half maximum (FWHM), especially for Q^2 and Q^3 components (>110 cm^{-1}), points to significant structural disorder and a broad distribution of local environments, consistent with a chemically complex, modifier-rich glass (Cassetta et al., 2021). Overall, the Raman fitting supports a strongly depolymerized and topologically heterogeneous silicate network, in agreement with the viscosity, fragility, and Boson-peak–derived nanoelastic descriptors (Pan et al., 2021).

Cross-polarized (HV) spectrum was acquired to isolate the Boson Peak while the air rotational Raman features and baseline were subtracted. The final spectrum was corrected using the Shuker and Gammon formalism (Shuker & Gammon, 1970). Thus, the experimental intensity I^{exp} can be expressed as reduced intensity I^{red}, as:

$$I^{red}(\omega) = \frac{I^{exp}}{\omega\,[n(\omega,T)+1]} = C(\omega)\,\frac{g(\omega)}{\omega^2}, \tag{4}$$

where $n(\omega,T) = \left[\exp\left(\frac{\hbar\omega}{k_B T}\right) - 1\right]^{-1}$ is the Bose-Einstein population factor $n(\omega,T)$, with k_B indicating the Boltzmann constant, $\hbar$ is the reduced Planck's constant, T the absolute temperature in kelvin, and $C(\omega)$ is the light-vibrations coupling function. Figure 3b reports the reduced low-ω spectrum.

The Boson peak (BP) observed at 78.5 cm^{-1} indicates a glass composition characterized by a relatively depolymerized network, consistent with a high fragility of the corresponding supercooled liquid. This conclusion is corroborated by both the MYEGA analysis and the model proposed in Cassetta et al. (2021), which independently classify the liquid as fragile. The Boson peak has long been recognized as a sensitive probe of medium-range order (MRO). Early studies established a close relationship between the Boson peak and the first sharp diffraction peak (FSDP, Börjesson et al., 1993; González-Jiménez et al., 2023; Kyotani et al., 2025; Kojima et al., 2020; Novikov & Sokolov, 1991) and linked it to nanoscale structural heterogeneity and elastic fluctuations. Accordingly, a higher BP frequency is generally associated with a weakly connected, highly disordered network characterized by reduced MRO (Cassetta et al., 2022, 2026; El Hamdaoui et al., 2023). Such a structural framework facilitates local rearrangements, a hallmark of fragile glass-forming systems. Furthermore, the elevated BP position points to the presence of rapid relaxation mechanisms, likely arising from low-energy vibrational excitations and anharmonic effects within the disordered network. These fast relaxation processes enable efficient dissipation of elastic energy on short timescales, reinforcing the interpretation of a fragile liquid. Within this framework, the BP serves as a spectroscopic indicator of structural softness and dynamic

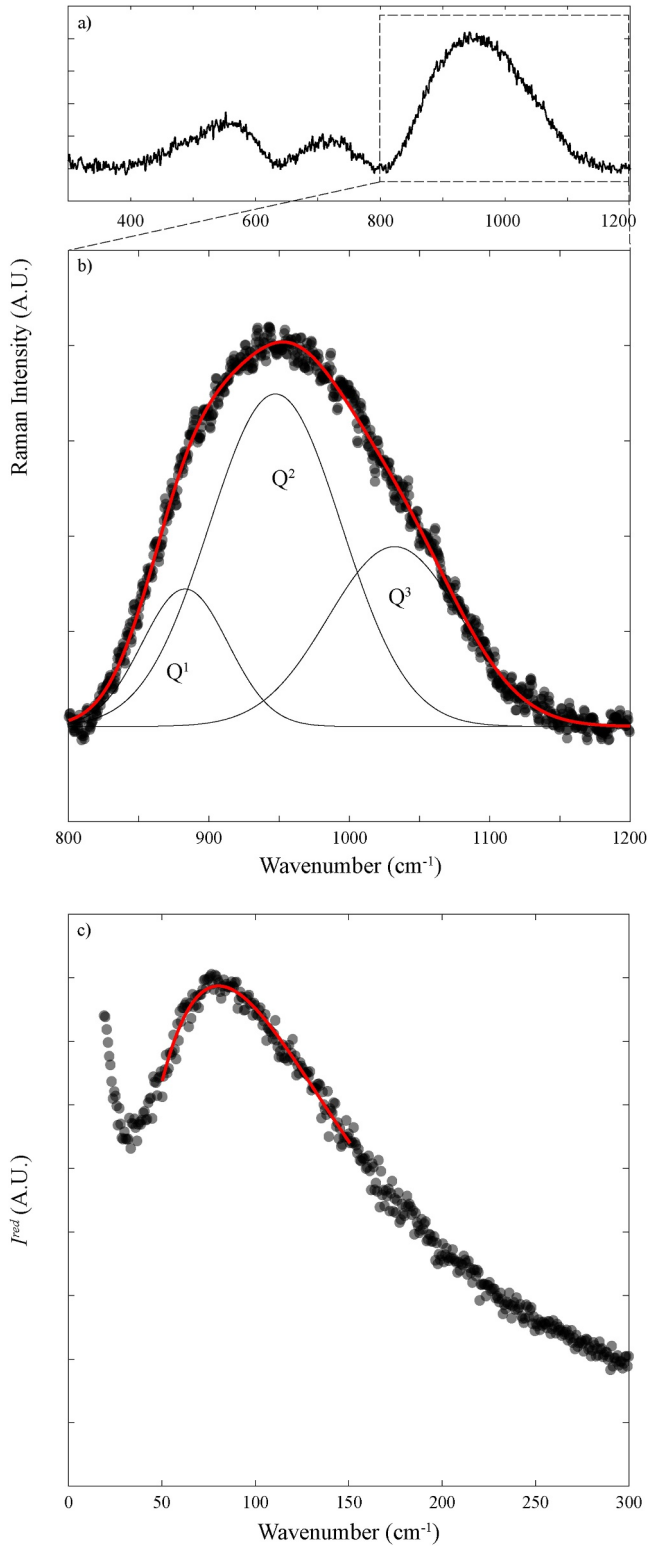

Figure 3. Raman spectral analysis of the investigated silicate glass. (a) Full-range Raman spectrum showing the main vibrational regions, with the dashed box highlighting the high-frequency domain associated with Si–O symmetric stretching vibrations. (b) Deconvolution of the (800–1,200 cm^{-1}) into individual Q^n structural units (black Gaussian curves). Black dots correspond to experimental data, and the red line represents the cumulative fit. (c) Low-frequency reduced Raman spectrum highlighting the Boson peak region. The red curve is the log-normal function used to fit the Boson peak profile in the form of $I(\omega) \propto \exp\left\{\frac{-\left[\ln\left(\frac{\omega}{\omega_{BP}}\right)\right]^2}{2\sigma^2}\right\}$, where σ is the BP width and ω_{BP} its position in cm^{-1}.

heterogeneity, both of which play a central role in the rapid loss of solid-like behavior as the system approaches the glass transition.

3.4. Elastic Properties

Longitudinal and transverse sound velocities were measured and used to calculate the elastic moduli of the doped glass. The longitudinal sound velocity (v_l) is 6,618 ± 21 m s^{-1}, while the transverse sound velocity (v_t) is 3,785 ± 11 m s^{-1}. The measured density is 2.831 ± 0.003 g cm^{-3}.

From these parameters, the elastic moduli were calculated via:

$$G = \rho v_t^2 \tag{5}$$

$$M = \rho v_l^2 \tag{6}$$

$$K = \rho\left(v_l^2 - \frac{4}{3}v_t^2\right) \tag{7}$$

$$E = \frac{9KG}{3K + G} \tag{8}$$

$$\upsilon = \frac{3K - 2G}{2(3K + G)}, \tag{9}$$

where the shear modulus (G) is 40.6 ± 0.2 GPa, the longitudinal modulus (M) is 124.0 ± 0.8 GPa, and the bulk modulus (K) is 69.9 ± 0.8 GPa. The Young's modulus (E) is 102.0 ± 0.5 GPa, and the Poisson's ratio (υ) is 0.26 ± 0.03.

Overall, the measured elastic parameters indicate a mechanically stiff glass, with well-constrained uncertainties and internal consistency among the calculated moduli (Rouxel, 2007).

4. Discussion

4.1. Impact of Fe-Mg-Ca Enrichment on Physical Properties of Basaltic Melts

To quantify the effect of Fe, Mg, and Ca increase on the rheology of a silicate melt starting from a basaltic composition, we compare the experimentally measured viscosities of the doped glass against the predicted viscosity of the parental basalt. To ensure a robust evaluation, the parental basalt viscosity was estimated using two distinct predictive frameworks: the empirical model of Giordano et al. (2008) and the more recent model by Langhammer et al. (2022). The comparison reveals a consistent viscosity decrease for the doped glass relative to the parental basalt in the high-T interval (1,428–1,299°C; Figure 2). In detail, the doped melt is, on average, ∼2.2 and ∼1.5 times less viscous than the parental basalt calculated by the models of Giordano et al. (2008) and Langhammer et al. (2022), respectively.

In contrast, within the low-T regime (678–639°C, Figure 2), the two models yield strikingly different scenarios. Comparison with the Giordano et al. (2008) model indicates a massive viscosity reduction, with the doped melt averaging a factor of ∼18.5 lower viscosity. Conversely, the Langhammer et al. (2022) model surprisingly displays a crossover with the experimental data of the doped melt.

The pronounced discrepancy and the observed low-T crossover strongly underscore the intrinsic complexity and uncertainty involved in accurately predicting the rheological behavior of even the starting parental composition near the glass transition. On one hand, the large viscosity gap shown by the Giordano et al. (2008) model may partly reflect an overestimation of the parental basalt viscosity. Several studies indicate that some experimental data sets used in these calibrations may be biased. Since this basaltic composition is reasonably prone to nanolite formation as observed for similar chemical compositions (e.g., Di Fiore et al., 2025), it is likely that comparable literature samples underwent nanolitization (e.g., Di Genova, Brooker et al., 2020; Joyce et al., 2021; Valdivia et al., 2025), resulting in systematically higher apparent viscosity values. Such a large discrepancy at low temperatures may be partially attributed to an overestimation of viscosity by the model of Giordano et al. (2008). On the other hand, the crossover highlights how different model formulations and calibration strategies can

fundamentally alter the baseline reference, emphasizing that estimating the viscosity of silicate melts remains a primary challenge in Earth and planetary sciences. However, the marked viscosity decrease estimated by both the empirical models is mainly attributable to the chemical enrichment in Fe, Mg, and Ca, particularly at temperatures above 800°C, which represent the most relevant thermal window for the magmatic evolution and effusive processes for planetary bodies. In particular, the addition of CaO and MgO effectively depolymerizes the silicate network (Giuliani et al., 2024; Neuville & Richet, 1991). This structural modification is quantitatively supported by the evolution of the NBO/T (non-bridging oxygens per tetrahedrally coordinated cation) and the activation energy (E_a) of the two melts. Assuming for comparison all iron as Fe^{2+}, the NBO/T values increase from 0.753 for the basalt to 1.401 for the doped sample. The significant rise in NBO/T confirms a more depolymerized structure in the doped melt, which is also reflected in a lower energy barrier for viscous flow. Correspondingly, the calculated activation energy for viscous flow decreases from 285 kJ/mol for the basalt to 248 kJ/mol for the doped melt. Among the doping oxides utilized, the influence of CaO could be the dominant driver for the viscosity decrement in the doped sample, as previously observed by Giuliani et al. (2024). In this study (Giuliani et al., 2024), the authors investigated the rheology of a Vesuvius phonotephrite doped with varying amounts of CaO and CaO + MgO, revealing that the addition of CaO alone reduces viscosity more effectively than the combined addition of CaO + MgO. The authors attribute this behavior to the high ionic potential of Mg^{2+} and its competition with Ca^{2+} for oxygen bonding, which inhibits the capacity of MgO to fully depolymerize the silicate network. Consequently, MgO addition is less effective in decreasing the melt viscosity.

This enrichment produces a marked decrease in melt viscosity, but also significantly affects the melt fragility. Melt fragility, commonly expressed by the parameter m, quantifies the steepness of the viscosity–temperature relationship in the vicinity of the glass transition temperature (T_g), and provides insight into the degree of structural cooperativity governing viscous flow (Mauro et al., 2009). Strong liquids exhibit low m values and near-Arrhenian behavior, whereas fragile liquids show high m values and a pronounced non-Arrhenian response.

By adopting the compositional dependence between ω_{BP} and melt chemistry, considering only the contribution of SiO_2 content, we estimate a $\omega_{BP} \sim 79.6\ cm^{-1}$ for the starting basalt, corresponding to a $m \sim 44$. This behavior demonstrates a consistent degree of agreement both with our estimates (Figure 2) and with previously reported non-linear relationships (highlighted in Cassetta et al., 2021; Cassetta et al., 2026), in which chemically driven parameters (m and ξ) approach constant values as melt compositions evolve from mafic to ultramafic regimes.

The enrichment in network-modifying cations enhances depolymerization (NBO/T = 1.4) and promotes a heterogeneous elastic landscape at the nanometer scale. Consistently, the nanoscale correlation length derived from the ratio between transverse sound velocity and boson peak frequency via:

$$\xi = \frac{v_t}{\omega_{BP}}, \tag{10}$$

where is $\xi = 1.82$ nm, indicating short-range nanoelastic heterogeneities and rapid growth of dynamical cooperativity upon cooling (e.g., the need for progressively larger groups of interconnected structural units to rearrange collectively during viscous flow, a hallmark of fragile glass-forming liquids, Adam & Gibbs, 1965).

Within this framework, the Boson peak acts as a vibrational fingerprint of fragility, linking elastic disorder, localized relaxation mechanisms, and the rapid loss of solid-like behavior approaching T_g (Cassetta et al., 2026). Overall, viscosity, fragility, and Raman observations converge toward a coherent picture in which chemical doping drives the melt into a highly fragile regime dominated by pronounced nanoelastic heterogeneities, distinct from the behavior of standard terrestrial basalts (Cassetta, Giannetta et al., 2023). These features are further strengthened by the full-range Raman response and the Q^n speciation, which independently point to a highly depolymerized and topologically heterogeneous silicate network. The low intensity of the ring (R) band, combined with its systematic shift toward higher wavenumbers (~560 cm^{-1}), indicates a predominance of small-membered rings (Le Losq et al., 2013). Such rings are intrinsically strained because closure of the ring requires significant deviation of the Si–O–Si bond angles from their energetically preferred configuration (e.g., quartz-like). The predominance of Q^2 units indicates a metasilicate-like network primarily composed of chain silicate structures, although Q^2 tetrahedra may also participate in ring configurations depending on the medium-range organization (Maekawa et al., 1991).

This structural configuration also provides a rationale for the measured elastic properties. Although the network is strongly depolymerized, the prevalence of chain-like Q^2 units can still ensure efficient local packing and connectivity along short silicate segments, while terminal Q^1 units associated with divalent cations (e.g., Fe^{2+}, Mg^{2+}, Ca^{2+}) contribute to local densification and strong ionic field effects (Cassetta et al., 2022; Mysen et al., 1982; Stabile et al., 2021). As a result, relatively high elastic moduli (M = 124.0 GPa, G = 40.6 GPa, K = 69.9 GPa, E = 102.0 GPa; ν = 0.26) can coexist with a fragmented network topology (Lin and Liu, 2006; Pan et al., 2021; Pisello et al., 2025). In this sense, the elevated stiffness reflects a compact and cation-stabilized local environment rather than extensive medium-range polymerization.

4.2. Evaluating Rheological Models Beyond Terrestrial Domains: Limits of Extrapolation and the Spectroscopy-Based Approach

To model the thermochemical evolution of rocky bodies and planetesimals in the Solar System, obtaining reliable viscosity constraints is of paramount importance, as viscosity directly dictates the kinetics of metal-silicate separation and the subsequent volcanic resurfacing processes. The melt composition investigated here represents a chemically exotic domain and therefore can be used as a critical benchmark for the predictive models routinely utilized to estimate the pure liquid viscosity of magmas (Cassetta et al., 2021; Giordano et al., 2008; Hui & Zhang, 2007; Langhammer et al., 2022; Le Losq et al., 2025; Sehlke & Whittington, 2016). Despite these models providing valuable insights, recent studies (Le Losq et al., 2025; Rai et al., 2019; Stapperfend et al., 2025) have highlighted significant limitations when applied to non-terrestrial compositions. Rai et al. (2019) observed that standard models can underestimate the viscosity of Ti-rich melts by up to 1.5 orders of magnitude. However, it is worth noting that their high temperature measurements were conducted also under high pressure conditions, and extrapolation to ambient pressure likely results in viscosity underestimation. In addition, Le Losq et al. (2025) emphasized that extrapolating terrestrial-calibrated models to Fe-rich planetary mantles can result in discrepancies reaching several orders of magnitude, due to the strong non-linear dependence of viscosity on chemical composition in these extreme regimes. Consistent with these observations, Raman studies of primitive planetary glasses have shown that highly depolymerized, Fe–Mg-rich compositions exhibit systematic shifts of the principal silicate bands relative to more polymerized glasses, reflecting distinct medium-range structural organizations that are not represented in conventional terrestrial calibration data sets (Le Losq & Sossi, 2023; Zeng et al., 2020). In the study of Stapperfend et al. (2025), in which the viscosity of the crystal-free melt of six lunar regolith simulants were characterized, was reported variable accuracy for the model by Giordano et al. (2008). In contrast, testing different models available in literature, they found the best agreement with the model by Sehlke and Whittington (2016), specifically calibrated that types of chemical compositions.

Furthermore, the metastable nature of supercooled melts makes them particularly prone to nanostructure formation and subsequent crystallization over timescales comparable to those of viscosity measurements (Di Genova et al., 2017; Di Genova, Brooker et al., 2020; Di Genova, Zandona, & Deubener, 2020; Okumura et al., 2022; Scarani et al., 2022; Valdivia et al., 2025; Verdurme et al., 2023). This behavior is especially pronounced in mafic melts, which are characterized by rapid crystallization kinetics (Arzilli et al., 2019; Di Fiore et al., 2021, 2024; Kolzenburg et al., 2022). These fast kinetics of crystallization for these magma compositions represent a major limitation for model reliability, as many existing data sets were acquired without systematic verification of the presence of nanoscale crystals.

For these reasons, we first assess the reliability of widely used semi-empirical viscosity models by benchmarking the predictions of the well-established viscosity models of Hui and Zhang (2007), Giordano et al. (2008), Sehlke and Whittington (2016), Cassetta et al. (2021), Langhammer et al. (2022) and Le Losq et al. (2025) against our new experimental viscosity data set, determining their predictive capability when extrapolated to this specific extraterrestrial planetary composition. The models mentioned above were implemented as follows:

1. The model proposed by Hui and Zhang (2007) is an empirical formulation designed to predict the viscosity of natural silicate melts over the entire experimental temperature range. To capture complex non-Arrhenian behavior, the authors utilized a specific functional form ((log η = A + B/T + exp(C + D/T)) involving four primary terms (A, B, C, D) related to temperature. However, to account for compositional dependence, each of these four terms is expressed as a linear function of oxide mole fractions (including a non-linear term for water), resulting in a total of 37 fitting parameters calibrated in the final model. The calibration was performed using a database of 1451 viscosity data points. This data set encompasses a wide range of "natural"

compositions, varying from rhyolite to peridotite, while explicitly excluding simple synthetic melts to ensure geological applicability;

2. The model of Giordano et al. (2008) predicts the non-Arrhenian viscosity of silicate melts as a function of temperature and composition. It employs the Vogel-Fulcher-Tammann (VFT) equation, optimizing a common high-temperature limit (A value fixed at −4.55) for all melts while ascribing compositional dependence to the B and C parameters via 18 model coefficients. The model is based on a database of more than 1770 viscosity measurements. This calibration data set covers a broad compositional spectrum, including 58 anhydrous melt compositions and 140 volatile-enriched melt compositions. However, as reported by many studies (Le Losq et al., 2025; Sehlke & Whittington, 2016; Stapperfend et al., 2025) its calibration data set is primarily focused on terrestrial magmatic rocks, leading it to drastically underestimate the viscosity of Mercurian, Martian, and Io compositions near the glass transition by up to four orders of magnitude. Furthermore, the authors of Giordano et al. (2008) reported in their study the poor predictive performances for high-titanium lunar mare basalts viscosity estimation by the model;
3. The model proposed by Sehlke and Whittington (2016) was developed specifically for planetary tholeiitic melts relevant to planetary surfaces. This model utilizes the Adam-Gibbs theory to relate viscosity to configurational entropy and temperature, employing a constant high-temperature limit and 12 adjustable sub-parameters to capture compositional dependence. The model was calibrated using 496 experimental viscosity data points obtained from 20 anhydrous tholeiitic compositions, 15 of which represent the surfaces of Mars, Mercury, the Moon, Io, and Vesta;
4. Distinct from the previous empirical models, Cassetta et al. (2021) proposed a method to estimate melt viscosity based on the vibrational properties of parental glasses, specifically correlating melt fragility (m) with the ratio of bulk to shear moduli (K/G) and the boson peak position (ω_{BP}). This approach allows for the derivation of viscosity curves using the MYEGA equation (Mauro et al., 2009) without direct high-temperature viscometry, thus avoiding crystallization issues common in unstable melts. The study characterized 16 anhydrous glasses and validated the method using a broader data set from the literature, totaling 43 samples (anhydrous and hydrous) and 278 viscosity data points for external validation;
5. Langhammer et al. (2022) introduced a machine learning approach utilizing an Artificial Neural Network (ANN) to map temperature and composition (including H_2O and iron redox state) directly to viscosity without assuming a fixed functional form. To overcome the experimental data gap at eruptive temperatures, the ANN is used to generate synthetic data in high- and low-viscosity ranges, which are then fitted with the physically motivated MYEGA equation (Mauro et al., 2009). The ANN was trained on a database of 3,482 viscosity data points derived from 153 distinct data sets, representing 320 unique compositions when accounting for variations in water content. Notably, this model has shown superior performance in predicting the glass transition temperature of lunar simulants compared to traditional models (Stapperfend et al., 2025) and similarly for some compositions of mixed-waste glass-forming melts (Stabile et al., 2025);
6. The more recent and comprehensive model was proposed by Le Losq et al. (2025). This model represents an advanced machine learning framework combining a "Graybox" neural network (embedding the VFT equation) with a Gaussian Process (GP) to predict viscosity and associated uncertainties. This model is designed to handle a vast range of conditions, including high pressure conditions (up to 30 GPa). The underlying database is extensive, containing 28,898 viscosity measurements. However, predictions from this model may become unreliable in extrapolative regimes, particularly for compositions with silica content below 50 mol%, where training data is sparse (Le Losq et al., 2025).

The temperature-dependence of the melt viscosities are reported in Figure 4, comparing the Vogel-Fulcher-Tammann (VFT) fit obtained from our experimental data (solid black line) with the empirical models described above. All models show a non-Arrhenian behavior of the viscosity curves (Figure 4), with the Hui and Zhang (2007) curve that shows a marked "linear-like trend", intercepting the VFT curve both at high-T and at low-T. This anomalous trend is attributed to the extrapolation of the model beyond its calibration database (Hui & Zhang, 2007); Interestingly, all other models underestimate the melt viscosity at high temperatures, with the notable exception of Cassetta et al. (2021), which exhibits a trend similar to the VFT fit but maintains consistently higher viscosity values across the entire high-T range. In the low-T range, the viscosity curves derived from the models of Langhammer et al. (2022) and Sehlke and Whittington (2016) continue to yield lower viscosity values compared to the VFT estimate. Conversely, the models by Giordano et al. (2008) and Le Losq et al. (2025) predict higher values than the experimental trend. This behavior results from the crossovers between these curves and the VFT fit occurring at approximately 698°C and 792°C for Giordano et al. (2008) and Le Losq et al. (2025),

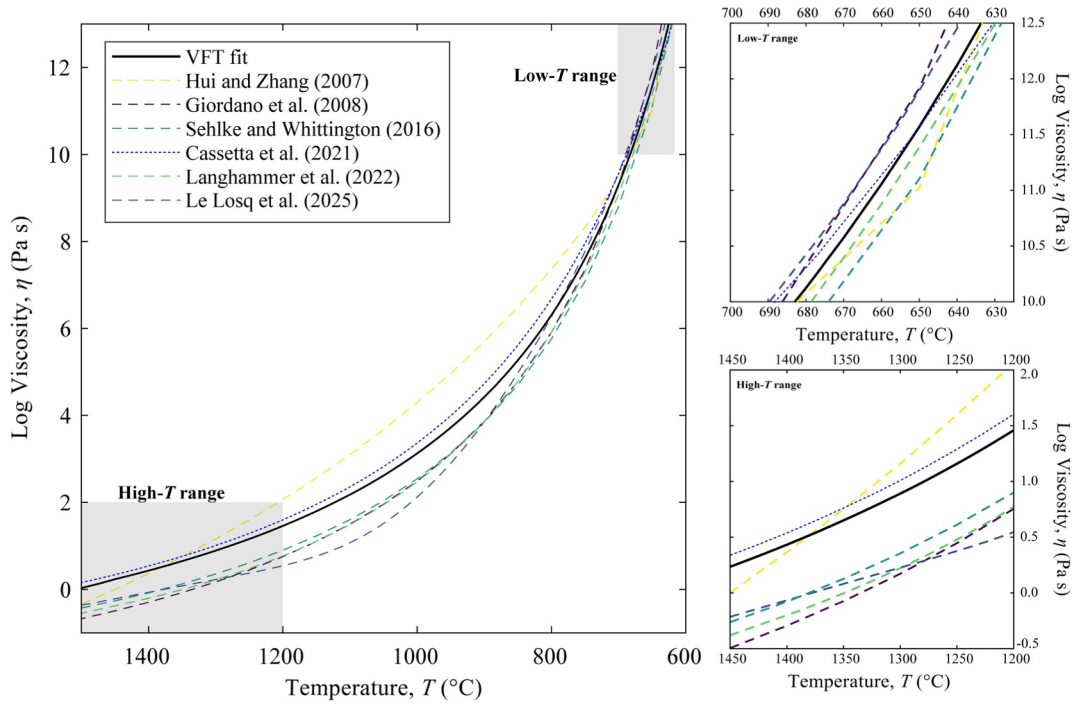

Figure 4. Statistical evaluation of model performance by comparing the estimated viscosity versus the VFT fit deriving from measured viscosity. Insets highlight the low-temperature and high-temperature ranges, illustrating the variable performance of existing models when extrapolated beyond terrestrial compositional domains.

respectively. Finally, the viscosity estimate from the model of Cassetta et al. (2021) crosses the VFT curve at 651°C; displaying below this temperature lower viscosity values, in contrast to the trend observed throughout the rest of the thermal range. To statistically evaluate the accuracy of the predicted viscosities, we calculated the RMSRE for the entire liquid viscosity data set, as well as separately for the high-T and low-T data. The results are reported in Figure 5 and Table 4. This analysis reveals that the model by Cassetta et al. (2021) returns the best overall RMSRE value of 0.13, while a RMSRE of 0.14 and 0.12 when considering the high-T range and low-T range separately (Table 4). In comparison, the model of Hui and Zhang (2007) shows the second-best overall RMSRE value of 0.35, with values of 0.12 and 0.48 for the high-T range and low-T range (Table 4), respectively. However, as observed in Figure 4 this calculated performance is an artifact resulting from the double crossover of the model viscosity trend with the VFT viscosity trend, coinciding with the viscosity-temperature range of the experimental measurements in this study. For the remaining viscosity models (Giordano et al., 2008; Langhammer et al., 2022; Le Losq et al., 2025; Sehlke & Whittington, 2016), the overall RMSRE values range from 0.46 to 0.57 (Figure 5 and Table 4). Focusing on the high-T range, these models exhibit similar performance, with RMSRE values spanning from 0.52 to 0.72 (Table 4). In contrast, in the low-T range the models of Langhammer et al. (2022) and Le Losq et al. (2025) yield better RMSRE values of 0.21 and 0.31, respectively, compared to the models of Giordano et al. (2008) and Sehlke and Whittington (2016), which display RMSRE of 0.35 and 0.48 (Table 4), respectively. The results from this comparison highlight that the 'exotic' nature of this chemical composition led to suboptimal model performance compared to their typical accuracy when estimating viscosities of compositions well-represented within their calibration databases. Interestingly, the exotic chemical regime explored in this study yields inferior results even when compared to other extraterrestrial planetary materials, such as lunar compositions. For instance, model benchmarks performed on lunar regolith measurements (Stapperfend et al., 2025) demonstrated better performance compared to our study for the models of Giordano et al. (2008), Sehlke and Whittington (2016), and Langhammer et al. (2022). This is likely due, in large part, to the sparse or non-existent representation of the chemical composition adopted in this study within the calibration data sets of the tested models, unlike the lunar regoliths analyzed by Stapperfend et al. (2025). Another notable result is the good performance of the spectroscopy-based viscosity model by Cassetta et al. (2021), which remains predictive even for chemically exotic, highly depolymerized melts. While the approach benefits from an independently measured T_g, this does not reduce its general applicability, because the departure from Arrhenian behavior

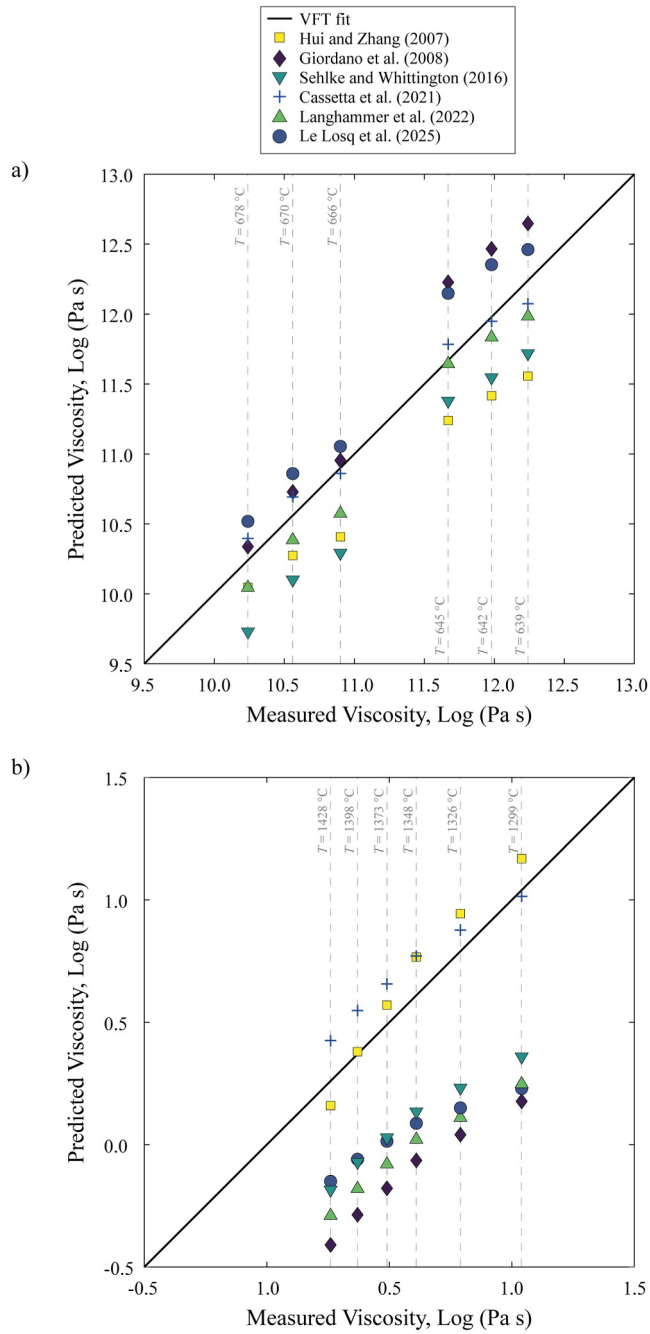

Figure 5. Predicted versus measured viscosity for the tested viscosity models. Panels compare model outputs with experimental viscosity values for the low-temperature range (a) and high-temperature range (b). The solid diagonal line marks the 1:1 correspondence between predicted and measured viscosity. Deviations from this line illustrate model errors (see also Table 4), with the spectroscopy-based approach (Cassetta et al., 2021) showing the closest overall agreement with the experimental data set.

(quantified by m) is embedded exclusively by the Boson peak descriptor. Indeed, the ability of a BP-based framework to reproduce the non-Arrhenian curvature of viscosity in Fe-, Mg-, and Ca-rich compositions again demonstrates that vibrational properties of glasses encode the fundamental physics governing melt dynamics, well beyond the limits of standard terrestrial and technical compositional domains (Cassetta, Mariotto et al., 2023; Cassetta, Vetere et al., 2023; Dominijanni et al., 2026; Giuliani et al., 2025; Stopponi et al., 2026).

Table 4
Results From the Comparison Between the Measured and Modeled Viscosities

T		η						
		Log (Pa s)						
(K)	(°C)	Measured	Hui and Zhang (2007)	Giordano et al. (2008)	Sehlke and Whittington (2016)	Cassetta et al. (2021)	Langhammer et al. (2022)	Le Losq et al. (2025)
1701	1428	0.26	0.16	−0.41	−0.18	0.43	−0.29	−0.15
1671	1398	0.37	0.38	−0.29	−0.07	0.55	−0.18	−0.06
1646	1373	0.49	0.57	−0.18	0.03	0.66	−0.08	0.01
1621	1348	0.61	0.77	−0.06	0.13	0.77	0.021	0.09
1599	1326	0.79	0.94	0.04	0.23	0.88	0.11	0.15
1572	1299	1.04	1.17	0.18	0.36	1.01	0.24	0.23
951	678	10.24	10.04	10.33	9.73	10.39	10.04	10.51
943	670	10.56	10.27	10.72	10.10	10.69	10.38	10.86
939	666	10.9	10.40	10.95	10.29	10.86	10.57	11.05
918	645	11.67	11.24	12.22	11.38	11.78	11.64	12.14
915	642	11.98	11.41	12.46	11.54	11.94	11.83	12.35
912	639	12.24	11.55	12.64	11.71	12.07	11.98	12.46

	RMSRE	Hui and Zhang (2007)	Giordano et al. (2008)	Sehlke and Whittington (2016)	Cassetta et al. (2021)	Langhammer et al. (2022)	Le Losq et al. (2025)
	High-T + Low-T	0.35	0.57	0.50	0.13	0.47	0.46
	High-T	0.12	0.72	0.52	0.14	0.63	0.57
	Low-T	0.48	0.35	0.48	0.12	0.21	0.31

5. Conclusions

This study demonstrates that the substantial enrichment of iron, magnesium, and calcium cations results in a pronounced depolymerization of the silicate domain under air-oxygen fugacity and atmospheric pressure. This structural modification drives a significant reduction in melt viscosity compared to typical terrestrial basalts. Raman spectroscopy confirms this fragmented topology through the dominance of Q^2 and Q^1 species. Interestingly, the high elastic moduli measured indicate that these terminal units and divalent cations facilitate local densification and high mechanical stiffness. Furthermore, the elevated Boson Peak frequency and high fragility values demonstrate that these exotic melts are characterized by highly non-Arrhenian dynamics and explained by their relatively small nanoelastic heterogeneities. Collectively, these observations explain why conventional viscosity models struggle to describe such compositionally extreme melts. Our benchmarking analysis reveals that traditional semi-empirical models, calibrated on data mainly based on terrestrial magmatic compositions, fail to accurately predict the rheology of such ultramafic systems, often leading to substantial predictive errors. In contrast, the success of the vibrational spectroscopy-based framework highlights that, at least for this case of study, nanoscale dynamics provide a more universal and robust descriptor for the physical evolution of non-terrestrial magmatic systems. In addition, these results provide essential constraints for modeling the thermo-chemical evolution and volcanic processes of chemically exotic planetary bodies. Finally, we highlight the necessity to generate new viscosity data sets including non-terrestrial chemical compositions of magma following rigorous experimental protocols that prevent or detect the onset of heterogeneities, particularly for these melt compositions that are prone to nanolitization.

Conflict of Interest

The authors declare no conflicts of interest relevant to this study.

Availability Statement

The data archiving is available on Figshare at the following DOI: https://doi.org/10.6084/m9.figshare.32261178.

Acknowledgments
F.D.F acknowledges funding from the MUR (Ministero dell'Università e della Ricerca) PNRR Project "Monitoring Earth Evolution and Tectonics" (MEET, Grant D53C22001400005). F.D.F. received additional support from INGV–Progetti Ricerca Libera: PANTA REI. M.C. acknowledges funding from ILGE-TNA/NOA-C2_030 – BOLLE and FINAL LAP - FINALizzazione intelligente dei materiali LAPidei derivanti da taglio - ID 54290 The authors would like to thank the Centre for Technological Platforms (CPT) of the University of Verona (Italy) for providing access to scientific instrumentation and technical support. The authors would like to thank Adrian Brown for the editorial handling. Special thanks are also due to Fabio Arzilli and an anonymous reviewer for their thorough and helpful reviews. Special thanks go to Elena Sofia Fanti for her valuable support with Raman measurements. Finally, the authors would like to express their gratitude to Lieutenant Commander Data of the USS Enterprise for inspiring them to dream of planets through science. Open access publishing facilitated by Istituto Nazionale di Geofisica e Vulcanologia, as part of the Wiley - CRUI-CARE agreement.

References

Adam, G., & Gibbs, J. H. (1965). On the temperature dependence of cooperative relaxation properties in glass-forming liquids. *Journal of Chemical Physics*, *43*(1), 139–146. https://doi.org/10.1063/1.1696442

Arzilli, F., La Spina, G., Burton, M. R., Polacci, M., Le Gall, N., Hartley, M. E., et al. (2019). Magma fragmentation in highly explosive basaltic eruptions induced by rapid crystallization. *Nature Geoscience*, *12*, 1023–1028. https://doi.org/10.1038/s41561-019-0468-6

Börjesson, L., Hassan, A. K., Swenson, J., Torell, L. M., & Fontana, A. (1993). Is there a correlation between the first sharp diffraction peak and the low frequency vibrational behavior of glasses? *Physical Review Letters*, *70*(9), 1275–1278. https://doi.org/10.1103/PhysRevLett.70.1275

Boukaré, C. É., Badro, J., & Samuel, H. (2025). Solidification of Earth's mantle led inevitably to a basal magma ocean. *Nature*, *640*(8057), 114–119. https://doi.org/10.1038/s41586-025-08701-z

Breuer, D., Spohn, T., Van Hoolst, T., van Westrenen, W., Stanley, S., & Rambaux, N. (2022). Interiors of earth-like planets and satellites of the solar system. *Surveys in Geophysics*, *43*(1), 177–226. https://doi.org/10.1007/s10712-021-09677-x

Cassetta, M., Di Genova, D., Zanatta, M., Boffa Ballaran, T., Kurnosov, A., Giarola, M., & Mariotto, G. (2021). Estimating the viscosity of volcanic melts from the vibrational properties of their parental glasses. *Scientific Reports*, *11*(1), 13072. https://doi.org/10.1038/s41598-021-92407-5

Cassetta, M., Giannetta, B., Enrichi, F., Zaccone, C., Mariotto, G., Giarola, M., et al. (2023). Effect of the alkali vs iron ratio on glass transition temperature and vibrational properties of synthetic basalt-like glasses. *Spectrochimica Acta Part A: Molecular and Biomolecular Spectroscopy*, *293*, 122430. https://doi.org/10.1016/j.saa.2023.122430

Cassetta, M., Mariotto, G., Daldosso, N., De Bona, E., Biesuz, M., Sorarù, G. D., et al. (2023). Viscosity, boson peak and elastic moduli in the Na_2O-SiO_2 system. *Minerals*, *13*(9), 1166. https://doi.org/10.3390/min13091166

Cassetta, M., Szewczyk, D., Giuliani, G., Dominijanni, S., Vetere, F., Iezzi, G., et al. (2026). Chemically driven Nano-Elastic heterogeneities control fragility in volcanic melts. *Advanced Science*, *13*(5), e12063. https://doi.org/10.1002/advs.202512063

Cassetta, M., Vetere, F., Zanatta, M., Perugini, D., Alvaro, M., Giannetta, B., et al. (2023). Micro-Raman spectroscopy for a comprehensive understanding of the structural evolution of Basaltic-Andesite and Trachybasalt multiphase systems. *Chemical Geology*, *616*, 121241. https://doi.org/10.1016/j.chemgeo.2022.121241

Cassetta, M., Zanatta, M., Biesuz, M., Giarola, M., & Mariotto, G. (2022). New insights about the role of Na–K ratio on the vibrational dynamics of synthetic-basalt glasses. *Journal of Raman Spectroscopy*, *53*(3), 540–549. https://doi.org/10.1002/jrs.6298

Demidova, S. I., & Badyukov, D. D. (2023). Peculiarities of the extraterrestrial basalts of the solar system with reference to the exoplanet science: A brief review. *Geochemistry International*, *61*(5), 453–467. https://doi.org/10.1134/S0016702923050038

Di Fiore, F., & Cassetta, M. (2026). Raw data of a fe-mg-ca enriched silicate melt. *Figshare*. https://doi.org/10.6084/m9.figshare.32261178

Di Fiore, F., Mollo, S., Vona, A., MacDonald, A., Ubide, T., Nazzari, M., et al. (2021). Kinetic partitioning of major and trace cations between clinopyroxene and phonotephritic melt under convective stirring conditions: New insights into clinopyroxene sector zoning and concentric zoning. *Chemical Geology*, *584*, 120531. https://doi.org/10.1016/j.chemgeo.2021.120531

Di Fiore, F., Pontesilli, A., Pozzi, G., Buono, G., Calabrò, L., Mollo, S., et al. (2026). Shear-induced crystallization as a trigger for rapid solidification of basalts: Implications for magma dynamics. *Earth and Planetary Science Letters*, *688*, 120116. https://doi.org/10.1016/j.epsl.2026.120116

Di Fiore, F., & Vona, A. (2026). Rheological evolution of a trachybasalt from mt. Etna under slow cooling. *Scientific Data*, *13*(1), 704. https://doi.org/10.1038/s41597-026-07048-y

Di Fiore, F., Vona, A., Costa, A., Mollo, S., & Romano, C. (2022). Quantifying the influence of cooling and shear rate on the disequilibrium rheology of a trachybasaltic melt from mt. Etna. *Earth and Planetary Science Letters*, *594*, 117725. https://doi.org/10.1016/j.epsl.2022.117725

Di Fiore, F., Vona, A., Di Genova, D., Caracciolo, A., Pontesilli, A., Calabrò, L., et al. (2025). Impact of cooling rate on rheology and emplacement dynamics of basaltic lavas: Insights from the January 2024 Sundhnúksgígar eruption (Iceland). *Journal of Volcanology and Geothermal Research*, *466*, 108400. https://doi.org/10.1016/j.jvolgeores.2025.108400

Di Fiore, F., Vona, A., Di Genova, D., Pontesilli, A., Calabrò, L., Mollo, S., et al. (2024). Magma titanium and iron contents dictate crystallization timescales and rheological behaviour in basaltic volcanic systems. *Communications Earth & Environment*, *5*(1), 283. https://doi.org/10.1038/s43247-024-01452-1

Di Fiore, F., Vona, A., Mollo, S., Nazzari, M., Giordano, G., & Romano, C. (2023). Experimental insights on the shear-induced crystallization of a phonotephrite magma. *Chemical Geology*, *637*, 121682. https://doi.org/10.1016/j.chemgeo.2023.121682

Di Fiore, F., Vona, A., Scarani, A., Giordano, G., Romano, C., Giordano, D., et al. (2023). Experimental constraints on the rheology of lavas from 2021 cumbre vieja eruption (La palma, Spain). *Geophysical Research Letters*, *50*(4), e2022GL100970. https://doi.org/10.1029/2022GL100970

Di Genova, D., Brooker, R. A., Mader, H. M., Drewitt, J. W. E., Longo, A., Deubener, J., et al. (2020). In situ observation of nanolite growth in volcanic melt: A driving force for explosive eruptions. *Science Advances*, *6*(39), eabb0413. https://doi.org/10.1126/sciadv.abb0413

Di Genova, D., Kolzenburg, S., Wiesmaier, S., Dallanave, E., Neuville, D. R., Hess, K. U., & Dingwell, D. B. (2017). A compositional tipping point governing the mobilization and eruption style of rhyolitic magma. *Nature*, *552*(7684), 235–238. https://doi.org/10.1038/nature24488

Di Genova, D., Zandona, A., & Deubener, J. (2020). Unravelling the effect of nano-heterogeneity on the viscosity of silicate melts: Implications for glass manufacturing and volcanic eruptions. *Journal of Non-Crystalline Solids*, *545*, 120248. https://doi.org/10.1016/j.jnoncrysol.2020.120248

Dominijanni, S., Calabrò, L., Bamber, E. C., Giuliani, G., Bondar, D., Valdivia, P., et al. (2026). Modeling magma viscosity and ascent dynamics of the 472 CE sub-Plinian eruption of Somma-Vesuvius (Italy). *Earth and Planetary Science Letters*, *673*, 119714. https://doi.org/10.1016/j.epsl.2025.119714

El Hamdaoui, A., Ghardi, E. M., Atila, A., Jabraoui, H., Badawi, M., Hasnaoui, A., & Ouaskit, S. (2023). The boson peak in silicate glasses: Insight from molecular dynamics. *Physical Chemistry Chemical Physics*, *25*(45), 31270–31280. https://doi.org/10.1039/D3CP02912C

Enrichi, F., Cassetta, M., Daldosso, N., Cattaruzza, E., Riello, P., Zairov, R., et al. (2023). Effect of the crystal structure on the optical properties and Ag sensitization of Tb3+/Yb3+ ions in silica-zirconia glasses and glass-ceramics. *Ceramics International*, *49*(24), 41064–41070. https://doi.org/10.1016/j.ceramint.2022.10.036

Galeener, F. L. (1979). Band limits and the vibrational spectra of tetrahedral glasses. *Physical Review B: Condensed Matter*, *19*(8), 4292–4297. https://doi.org/10.1103/PhysRevB.19.4292

Giordano, D., & Russell, J. K. (2007). A rheological model for glassforming silicate melts in the systems CAS, MAS, MCAS. *Journal of Physics: Condensed Matter*, *19*(20), 205148. https://doi.org/10.1088/0953-8984/19/20/205148

Giordano, D., Russell, J. K., & Dingwell, D. B. (2008). Viscosity of magmatic liquids: A model. *Earth and Planetary Science Letters*, *271*(1–4), 123–134. https://doi.org/10.1016/j.epsl.2008.03.038

Giuliani, G., Calabrò, L., Stopponi, V., Bondar, D., Abeykoon, S., Romano, C., et al. (2025). Aluminum control on viscosity and structure of haplogranitic melts: Implications for rhyolitic melt viscosity determination. *Chemical Geology*, *698*, 123127. https://doi.org/10.1016/j.chemgeo.2025.123127

Giuliani, G., Di Genova, D., Di Fiore, F., Valdivia, P., Mollo, S., Romano, C., et al. (2024). The effect of carbonate assimilation and nano-heterogeneities on the viscosity of phonotephritic melt from Vesuvius. *Chemical Geology*, *670*, 122408. https://doi.org/10.1016/j.chemgeo.2024.122408

Glazner, A. F. (2014). Magmatic life at low Reynolds number. *Geology*, *42*(11), 935–938. https://doi.org/10.1130/G36078.1

González-Jiménez, M., Barnard, T., Russell, B. A., Tukachev, N. V., Javornik, U., Hayes, L. A., et al. (2023). Understanding the emergence of the boson peak in molecular glasses. *Nature Communications*.

Goodrich, C. A., & Delaney, J. S. (2000). Fe/Mg–Fe/Mn relations of meteorites and primary heterogeneity of primitive achondrite parent bodies. *Geochimica et Cosmochimica Acta*, *64*(1), 149–160. https://doi.org/10.1016/S0016-7037(99)00107-6

Gottsmann, J., Giordano, D., & Dingwell, D. B. (2002). Predicting shear viscosity during volcanic processes at the glass transition: A calorimetric calibration. *Earth and Planetary Science Letters*, *198*(3–4), 417–427. https://doi.org/10.1016/S0012-821X(02)00522-8

Hamano, K., Abe, Y., & Genda, H. (2013). Emergence of two types of terrestrial planet on solidification of magma ocean. *Nature*, *497*(7451), 607–610. https://doi.org/10.1038/nature12163

Herzberg, C., Condie, K., & Korenaga, J. (2010). Thermal history of the Earth and its petrological expression. *Earth and Planetary Science Letters*, *292*(1–2), 79–88. https://doi.org/10.1016/j.epsl.2010.01.022

Hui, H., & Zhang, Y. (2007). Toward a general viscosity equation for natural anhydrous and hydrous silicate melts. *Geochimica et Cosmochimica Acta*, *71*(2), 403–416. https://doi.org/10.1016/j.gca.2006.09.003

Joyce, A., Kmiec, S., & Martin, S. W. (2021). Glass transition temperature studies of planetary ball milled glasses: Accessing the rapidly cooled glassy state in Na4P2S7-xOx, $0 \leq x \leq 7$, Oxy-thio phosphate glasses. *Journal of Non-Crystalline Solids*, *551*, 120462. https://doi.org/10.1016/j.jnoncrysol.2020.120462

Keil, K. (2012). Angrites, a small but diverse suite of ancient, silica-undersaturated volcanic-plutonic mafic meteorites, and the history of their parent asteroid. *Chemie der Erde*, *72*(3), 191–218. https://doi.org/10.1016/j.chemer.2012.06.002

Kleine, T., Hans, U., Irving, A. J., & Bourdon, B. (2012). Chronology of the angrite parent body and implications for core formation in protoplanets. *Geochimica et Cosmochimica Acta*, *84*, 186–203. https://doi.org/10.1016/j.gca.2012.01.032

Kojima, S., Novikov, V. N., Kofu, M., & Yamamuro, O. (2020). Nanometric fluctuations of sound velocity in Alkali borate glasses and fragility of respective melts. *Physica Status Solidi (B) Basic Research*, *257*(11), 2000073. https://doi.org/10.1002/PSSB.202000073

Kolzenburg, S., Chevrel, M. O., & Dingwell, D. B. (2022). Magma/suspension rheology. *Reviews in Mineralogy and Geochemistry*, *87*(1), 639–720. https://doi.org/10.2138/rmg.2022.87.14

Kyotani, D., Oh, S. H., Kitani, S., Fujii, Y., Hijiya, H., Mizuno, H., et al. (2025). Relationship between the boson peak and first sharp diffraction peak in glasses. *Scientific Reports 2025*, *15*(1), 9617. https://doi.org/10.1038/s41598-025-94454-8

Langhammer, D., Di Genova, D., & Steinle-Neumann, G. (2022). Modeling viscosity of volcanic melts with artificial neural networks. *Geochemistry, Geophysics, Geosystems*, *23*(12), e2022GC010673. https://doi.org/10.1029/2022GC010673

Lark, L. H., Huber, C., Parmentier, E. M., & Head, J. W. (2024). Planetary Interior configuration control on thermal evolution and geological history. *Journal of Geophysical Research: Planets*, *129*(11), e2024JE008361. https://doi.org/10.1029/2024JE008361

Le Losq, C., Ferraina, C., Sossi, P. A., & Boukaré, C.-É. (2025). A general machine learning model of aluminosilicate melt viscosity and its application to the surface properties of dry lava planets. *Earth and Planetary Science Letters*, *656*, 119287. https://doi.org/10.1016/j.epsl.2025.119287

Le Losq, C., Neuville, D. R., Florian, P., Henderson, G. S., & Massiot, D. (2013). The role of Al^{3+} on rheology and structural changes in sodium silicate and aluminosilicate glasses and melts. *Geochimica et Cosmochimica Acta*, *126*, 495–517. https://doi.org/10.1016/j.gca.2013.11.010

Le Losq, C., & Sossi, P. A. (2023). Atomic structure and physical properties of peridotite glasses at 1 bar. *Frontiers in Earth Science*, *11*, 1040750. https://doi.org/10.3389/feart.2023.1040750

Lin, C.-C., & Liu, L. (2006). Composition dependence of elasticity in aluminosilicate glasses. *Physics and Chemistry of Minerals*, *33*(5), 332–346. https://doi.org/10.1007/s00269-006-0084-z

Maekawa, H., Maekawa, T., Kawamura, K., & Yokokawa, T. (1991). The structural groups of alkali silicate glasses determined from 29Si MAS-NMR. *Journal of Non-Crystalline Solids*, *127*(1), 53–64. https://doi.org/10.1016/0022-3093(91)90400-Z

Marchi, S., & Korenaga, J. (2025). The shaping of terrestrial planets by late accretions. *Nature*, *641*(8065), 1111–1120. https://doi.org/10.1038/s41586-025-08970-8

Marchi, S., Rufu, R., & Korenaga, J. (2023). Long-lived volcanic resurfacing of Venus driven by early collisions. *Nature Astronomy*, *7*(10), 1180–1187. https://doi.org/10.1038/s41550-023-02037-2

Mauro, J. C., Yue, Y., Ellison, A. J., Gupta, P. K., & Allan, D. C. (2009). Viscosity of glass-forming liquids. *Proceedings of the National Academy of Sciences*, *106*(47), 19780–19784. https://doi.org/10.1073/pnas.0911705106

Mysen, O., Finger, L. W., Virgo, D., & Seifert, A. F. (1982). Curve-fitting of Raman spectra of silicate glasses. *American Mineralogist*.

Neuville, D. R., & Richet, P. (1991). Viscosity and mixing in molten (Ca, Mg) pyroxenes and garnets. *Geochimica et Cosmochimica Acta*, *55*(4), 1011–1019. https://doi.org/10.1016/0016-7037(91)90159-3

Novikov, V. N., & Sokolov, A. P. (1991). A correlation between low-energy vibrational spectra and first sharp diffraction peak in chalcogenide glasses. *Solid State Communications*, *77*(3), 243–247. https://doi.org/10.1016/0038-1098(91)90341-R

Okumura, S., Uesugi, K., Goto, A., Sakamaki, T., Matsumoto, K., Takeuchi, A., & Miyake, A. (2022). Rheology of nanocrystal-bearing andesite magma and its roles in explosive volcanism. *Communications Earth & Environment*, *3*(1), 241. https://doi.org/10.1038/s43247-022-00573-9

Pan, Z., Benzine, O., Sawamura, S., Limbach, R., Koike, A., Bennett, T. D., et al. (2021). Disorder classification of the vibrational spectra of modern glasses. *Physical Review B*, *104*(13), 134106. https://doi.org/10.1103/PhysRevB.104.134106

Pisello, A., Corezzi, S., Cassetta, M., Radica, F., Comez, L., Iezzi, G., et al. (2025). Brillouin spectroscopy of natural and chemically complex volcanic glasses: The role of divalent cations. *Chemical Geology*, *681*, 122719. https://doi.org/10.1016/j.chemgeo.2025.122719

Rai, N., Perrillat, J.-P., Mezouar, M., Colin, A., Petitgirard, S., & van Westrenen, W. (2019). In situ viscometry of primitive lunar magmas at high pressure and high temperature. *Frontiers in Earth Science*, *7*, 94. https://doi.org/10.3389/feart.2019.00094

Rouxel, T. (2007). Elastic properties and short-to medium-range order in glasses. *Journal of the American Ceramic Society*, *90*(10), 3019–3039. https://doi.org/10.1111/j.1551-2916.2007.01945.x

Russell, J. K., Hess, K.-U., & Dingwell, D. B. (2022). Models for viscosity of geological melts. *Reviews in Mineralogy and Geochemistry*, *87*(1), 841–885. https://doi.org/10.2138/rmg.2022.87.18

Scarani, A., Zandonà, A., Di Fiore, F., Valdivia, P., Putra, R., Miyajima, N., et al. (2022). A chemical threshold controls nanocrystallization and degassing behaviour in basalt magmas. *Communications Earth & Environment*, *3*(1), 284. https://doi.org/10.1038/s43247-022-00615-2

Schaefer, L., & Elkins-Tanton, L. T. (2018). Magma oceans as a critical stage in the tectonic development of rocky planets. In *Philosophical transactions of the Royal Society A: Mathematical, physical and engineering sciences*. Royal Society Publishing. https://doi.org/10.1098/rsta.2018.0109

Sehlke, A., & Whittington, A. G. (2016). The viscosity of planetary tholeiitic melts: A configurational entropy model. *Geochimica et Cosmochimica Acta*, *191*, 277–299. https://doi.org/10.1016/j.gca.2016.07.027

Shuker, R., & Gammon, R. W. (1970). Raman-Scattering selection-rule breaking and the density of States in amorphous materials. *Physical Review Letters*, *25*(4), 222–225. https://doi.org/10.1103/PhysRevLett.25.222

Stabile, P., Fornasini, L., Pasetti, L., Bersani, D., Dominijanni, S., di Genova, D., et al. (2025). Characterization of mixed-waste glasses in the CAS system: Insights from differential scanning calorimetry and Raman spectroscopy. *The European Physical Journal Plus*, *140*(8), 739. https://doi.org/10.1140/epjp/s13360-025-06677-3

Stabile, P., Sicola, S., Giuli, G., Paris, E., Carroll, M. R., Deubener, J., & Di Genova, D. (2021). The effect of iron and alkali on the nanocrystal-free viscosity of volcanic melts: A combined Raman spectroscopy and DSC study. *Chemical Geology*, *559*, 119991. https://doi.org/10.1016/j.chemgeo.2020.119991

Stapperfend, S., Dingwell, D. B., Hess, K.-U., Sutherland, J., Müller, A., Müller, D., et al. (2025). Viscosity measurements of selected lunar regolith simulants. *American Mineralogist*, *110*(8), 1171–1185. https://doi.org/10.2138/am-2023-9263

Stevenson, R. J., Dingwell, D. B., Webb, S. L., & Bagdassarov, N. S. (1995). The equivalence of enthalpy and shear stress relaxation in rhyolitic obsidians and quantification of the liquid-glass transition in volcanic processes. *Journal of Volcanology and Geothermal Research*, *68*(4), 297–306. https://doi.org/10.1016/0377-0273(95)00015-1

Stopponi, V., Giuliani, G., Calabrò, L., Bondar, D., Abeykoon, S., Romano, C., et al. (2026). Viscosity and structure of Na_2O-enriched haplogranitic melts: A DSC shift-factor calibration for peralkaline rhyolites. *Chemical Geology*, *702*, 123196. https://doi.org/10.1016/j.chemgeo.2025.123196

Su, X., Liu, J., Zhou, Y., Hu, J., Roskosz, M., & Lin, J. (2025). Sound velocities of basaltic glass at Earth's deep-mantle pressures. *Geochemistry, Geophysics, Geosystems*, *26*(8), e2025GC012272. https://doi.org/10.1029/2025GC012272

Szewczyk, D., & Cassetta, M. (2024). Colossal low-temperature upturn in the heat capacity of volcanic glasses. *Journal of Non-Crystalline Solids*, *637*, 123046. https://doi.org/10.1016/j.jnoncrysol.2024.123046

Tammann, G. H. W. Z., & Hesse, W. (1926). The dependence of viscosity upon the temperature of supercooled liquids. *Zeitschrift fuer Anorganische und Allgemeine Chemie*, *156*(1), 245–257.

Tryggvason, E. (1986). Multiple magma reservoirs in a rift zone volcano: Ground deformation and magma transport during the September 1984 eruption of Krafla, Iceland. *Journal of Volcanology and Geothermal Research*, *28*(1–2), 1–44. https://doi.org/10.1016/0377-0273(86)90003-X

Valdivia, P., Zandonà, A., Löschmann, J., Bondar, D., Genevois, C., Canizarès, A., et al. (2025). Nanoscale chemical heterogeneities control the viscosity of andesitic magmas. *Communications Earth & Environment*, *6*(1), 455. https://doi.org/10.1038/s43247-025-02424-9

Verdurme, P., le Losq, C., Chevrel, O., Pannefieu, S., Médard, E., Berthod, C., et al. (2023). Viscosity of crystal-free silicate melts from the active submarine volcanic chain of Mayotte. *Chemical Geology*, *620*, 121326. https://doi.org/10.1016/j.chemgeo.2023.121326

Weiss, B. P., & Elkins-Tanton, L. T. (2013). Differentiated planetesimals and the parent bodies of chondrites. *Annual Review of Earth and Planetary Sciences*, *41*(1), 529–560. https://doi.org/10.1146/annurev-earth-040610-133520

Wu, L., Yang, D.-B., Xie, H.-S., Li, F.-F., Hu, B., Yu, Y., et al. (2014). Pressure-induced elastic and structural changes in hydrous basalt glasses: The effect of H2O on the gravitational stability of basalt melts at the base of the upper mantle. *Earth and Planetary Science Letters*, *406*, 165–173. https://doi.org/10.1016/j.epsl.2014.09.006

Zandonà, A., Scarani, A., Löschmann, J., Cicconi, M. R., Di Fiore, F., de Ligny, D., et al. (2023). Non-stoichiometric crystal nucleation in a spodumene glass containing TiO2 as seed former: Effects on the viscosity of the residual melt. *Journal of Non-Crystalline Solids*, *619*, 122563. https://doi.org/10.1016/j.jnoncrysol.2023.122563

Zeng, X., Li, X., Liu, J., Mo, B., Yu, W., & Tang, H. (2020). Discerning lunar pyroclastic and impact glasses via raman spectroscopy. *Journal of Geophysical Research: Planets*, *125*(12), e2020JE006674. https://doi.org/10.1029/2020JE006674